*promoting access to White Rose research papers*

**Universities of Leeds, Sheffield and York**
**http://eprints.whiterose.ac.uk/**

This is an author produced version of a paper published in **IEEE Transactions on Geoscience and Remote Sensing**.

White Rose Research Online URL for this paper:
http://eprints.whiterose.ac.uk/43175

**Published paper**

Chen, J., Quegan, S., *Calibration of spaceborne CTLR compact polarimetric low-frequency SAR using mixed radar calibrators*, IEEE Transactions on Geoscience and Remote Sensing, 49 (7), pp. 2712-2723
http://dx.doi.org/10.1109/TGRS.2011.2109065

*White Rose Research Online*
*eprints@whiterose.ac.uk*

# Calibration of Spaceborne CTLR Compact Polarimetric Low Frequency SAR Using Mixed Radar Calibrators

Jie Chen [(1)], *Member, IEEE,* Shaun Quegan [(2)], *Member, IEEE*

(1) School of Electronic and Information Engineering, Beihang University (BUAA), Beijing, 100191, China

e-mail: chenjie@buaa.edu.cn; Jie.Chen@sheffield.ac.uk

(2) School of Mathematics and Statistics, University of Sheffield, Sheffield, S37RH, UK

e-mail: s.quegan@sheffield.ac.uk

***Abstract*—Spaceborne synthetic aperture radar (SAR) systems operating at lower frequencies, such as P-band, are significantly affected by Faraday rotation (FR) effects. A novel algorithm for calibrating the circular transmit and linear receive mode spaceborne compact polarimetric SAR using mixed calibrators is proposed, which is able to correct precisely both FR and radar system errors (i.e. channel imbalance and cross-talk). Six sets of mixed calibrators, consisting of both passive calibrators and polarimetric active radar calibrators (PARCs), are investigated. Theoretical analysis and simulations demonstrate that the optimal calibration scheme combines four polarimetric selective mixed calibrators, including two gridded trihedrals and two PARCs, together with total electron content measurements by the GNSS system.**

***Index Terms*— Calibration, Faraday rotation, Ionosphere, Compact polarimetry, Synthetic aperture radar (SAR).**

## I. INTRODUCTION

There is growing interest in deploying lower frequency spaceborne Synthetic Aperture Radars (SARs) for monitoring of the Earth, such as the P-band BIOMASS mission to measure forest biomass [1], which is currently under Phase-A study by the European Space Agency. However, the ionosphere can

significantly affect such systems; in particular, L- and P-band spaceborne SAR measurements will suffer from Faraday rotation (FR) [1]–[4]. Furthermore, two conflicting factors often affect the design of such systems, namely the need for frequent global coverage and the need to maximize information content, which often requires polarimetric information. Full polarimetry (FP) suffers from reduced swath width compared to SAR systems transmitting on a single polarization, thus increasing the time needed for global coverage. As a result, there has been growing interest in the compact polarimetric (CP) SAR mode [5]-[14], because, for a given swath width, it operates with reduced data rate, system power and pulse repetition frequency compared to a FP system, while still allowing estimates of some of the key polarimetric quantities.

The first system of this type, proposed by Souyris *et al*. [5], [6], used the $\pi/4$ CP mode, which transmits H+V ($45^o$ linearly polarized) and receives echoes in the H and V polarizations. However, such a system could also be severely affected by FR [11]–[14]. A way to reduce the effects of FR was suggested by Raney [8] when he introduced the hybrid mode (also called the $\pi/2$ mode [11] or CTLR mode [12]) which transmits on circular polarization and receives on the two linear (H, V) polarizations. This is a promising approach, since circular polarizations are preserved under FR [6], [10], [12] and [13]; hence the polarization of the incident wave would be undistorted and only FR effects on the return signal would need to be corrected.

Freeman [14] developed a system model for CTLR mode compact polarimetry with FR. On the basis of this model, this paper proposes a novel algorithm for calibrating the CTLR mode using both passive and active calibration targets. After an introduction to the system model in Section II, the mathematical analysis in Section III leads to a set of new calibration algorithms and an optimized set of calibrators. Computer simulations presented in Section IV verify the effectiveness of the approach; these include simulations accounting just for radar system errors and FR, and simulations that also take calibrator

errors into account.

## II. System Model for CTLR Compact Polarimetry

### A. Faraday Rotation

When a polarized electromagnetic wave traverses the ionosphere, its interaction with free electrons and the Earth's magnetic field leads to rotation of the polarization vector [4], [15]. This phenomenon is known as Faraday rotation. The one-way FR for a SAR signal can be approximated as [15]

$$\Omega = \frac{K}{f_0^2} \cdot \left[ B \cos\psi \cdot \sec\theta \right]_{400} \cdot \mathrm{TEC} \tag{1}$$

where $f_0$ is the carrier frequency in Hz, $K$ is a constant of value $2.365\times10^4$ [A·m$^2$/kg], $B$ is the magnetic flux density in Wb/m$^2$, and $\psi$ and $\theta$ are the angles the wave-normal makes with the Earth's magnetic field and the downward vertical, respectively. TEC is the total electron content in TEC units (1 TECU = $10^{16}$ electrons m$^{-2}$). The "magnetic field factor", $\left[ B\cos\psi \cdot \sec\theta \right]_{400}$, is calculated at a height of 400 km.

### B. System Model

We assume a CTLR mode SAR system that transmits right-circular polarization chirps and receives linear (H, V) polarization echoes. In the presence of cross-talk, the transmitted electric field will include a component from the orthogonal left-circular polarization, so has the form [14]

$$\begin{bmatrix} T_H \\ T_V \end{bmatrix} = \frac{1}{\sqrt{2}} \left\{ \begin{bmatrix} 1 \\ -j \end{bmatrix} + \delta_c \begin{bmatrix} 1 \\ j \end{bmatrix} \right\} = \frac{1}{\sqrt{2}} \begin{bmatrix} 1+\delta_c \\ -j(1-\delta_c) \end{bmatrix}$$

where $\delta_c$ is a cross-talk parameter.

With Faraday rotation, Ω, the electric field incident on the Earth's surface will be [14]

$$\begin{bmatrix} E_H^i \\ E_V^i \end{bmatrix} = \begin{bmatrix} \cos\Omega & \sin\Omega \\ -\sin\Omega & \cos\Omega \end{bmatrix} \cdot \begin{bmatrix} T_H \\ T_V \end{bmatrix} = \frac{1}{\sqrt{2}} \begin{bmatrix} e^{-j\Omega} + \delta_c e^{j\Omega} \\ -j\left( e^{-j\Omega} - \delta_c e^{j\Omega} \right) \end{bmatrix} \tag{2}$$

Freeman [14] introduced a system model for this CTLR mode, in which the measured scattering vectors are given by

$$\begin{bmatrix} M_{RH} \\ M_{RV} \end{bmatrix} = A(r,\theta)e^{j\varphi} \cdot \frac{1}{\sqrt{2}} \begin{bmatrix} 1 & \delta_2 \\ \delta_1 & f \end{bmatrix} \cdot \begin{bmatrix} \cos\Omega & \sin\Omega \\ -\sin\Omega & \cos\Omega \end{bmatrix} \cdot \begin{bmatrix} S_{HH} & S_{HV} \\ S_{VH} & S_{VV} \end{bmatrix} \cdot \begin{bmatrix} e^{-j\Omega} + \delta_c e^{j\Omega} \\ -j\left(e^{-j\Omega} - \delta_c e^{j\Omega}\right) \end{bmatrix} + \begin{bmatrix} N_1 \\ N_2 \end{bmatrix} \tag{3}$$

where $S_{HH}$, $S_{HV}$, $S_{VH}$ and $S_{VV}$ are the components of the true scattering matrix, $M_{RH}$ and $M_{RV}$ are the components of the measured scattering vector, $f$ denotes channel imbalance, $\delta_i$, $i$ = 1-2, are crosstalk terms in the receiving channel, and $N_i$, $i$ = 1-2, are additive noise terms present in each measurement.

## III. CALIBRATION ALGORITHM VIA MIXED CALIBRATORS

### *A. Signatures of Mixed Calibrators*

By mixed calibrators we refer to a set of passive and active radar calibrators operating in combination. Their use for calibrating spaceborne FP SAR systems is discussed in [16]-[22]. Passive radar calibrators usually consist of the dihedral, trihedral and gridded trihedral (the classical trihedral with gridded base wires or thin plates [22], see Fig.1(c)), while the polarimetric active radar calibrators (PARCs) include three types [16], denoted as $\text{PARC}_\text{X}$, $\text{PARC}_\text{Y}$ and $\text{PARC}_\text{P}$, respectively, having signature matrices:

$$\mathbf{S}_X = \begin{bmatrix} 0 & 0 \\ 1 & 0 \end{bmatrix} \qquad \mathbf{S}_Y = \begin{bmatrix} 0 & 1 \\ 0 & 0 \end{bmatrix} \qquad \mathbf{S}_P = \begin{bmatrix} 1 & 1 \\ -1 & -1 \end{bmatrix} \tag{4}$$

where $\text{PARC}_\text{X}$ and $\text{PARC}_\text{Y}$ are polarimetric selective active calibrators.

For the passive calibrators illustrated in Fig.1, the scattering matrixes can be written as [22]

$$[\mathbf{S}_{Tri}] = A_{Tri}(\theta,\phi) \cdot e^{j\varphi_{Tri}(\theta,\phi)} \cdot \begin{bmatrix} 1 & 0 \\ 0 & 1 \end{bmatrix} \tag{5}$$

$$[\mathbf{S}_{Di}] = A_{Di}(\theta,\phi) \cdot e^{j\varphi_{Di}(\theta,\phi)} \cdot \begin{bmatrix} \cos 2\psi & \sin 2\psi \\ \sin 2\psi & -\cos 2\psi \end{bmatrix} \tag{6}$$

$$[\mathbf{S}_{Gt}] = \frac{A_{Gt}(\theta,\phi) \cdot e^{j\varphi_{Gt}(\theta,\phi)}}{\sin^2\phi + \cos^2\phi \cdot \sin^2\theta} \cdot \begin{bmatrix} \sin^2\phi & -\sin\phi\cos\phi\sin\theta \\ -\sin\phi\cos\phi\sin\theta & \cos^2\phi \cdot \sin^2\theta \end{bmatrix} \tag{7}$$

where $A_{Tri}$, $A_{Di}$ and $A_{Gt}$ are gain factors, $\varphi_{Tri}$, $\varphi_{Di}$ and $\varphi_{Gt}$ are phase factors, $\phi$ and $\theta$ are the azimuth and elevation angles, and $\psi$ is the rotation angle of the dihedral.

Without loss of generality, we assume that the gain and phase factors in the ideal responses of (4)-(7) are known, and can be normalized for simplicity. Then we have

$$\mathbf{S}_{Tri} = \begin{bmatrix} 1 & 0 \\ 0 & 1 \end{bmatrix} \qquad \mathbf{S}_{Di} = \begin{bmatrix} 1 & 0 \\ 0 & -1 \end{bmatrix} \qquad \mathbf{S}_{Gt1} = \begin{bmatrix} 1 & 0 \\ 0 & 0 \end{bmatrix} \qquad \mathbf{S}_{Gt2} = \begin{bmatrix} 0 & 0 \\ 0 & 1 \end{bmatrix} \tag{8}$$

where $\mathbf{S}_{Tri}$, $\mathbf{S}_{Di}$, $\mathbf{S}_{Gt1}$ and $\mathbf{S}_{Gt2}$ denote the signature matrices of the trihedral, dihedral ($\psi$ = 0) and gridded

trihedrals Gt1 ($\phi = \pi/2$, vertical grid) and Gt2 ($\phi = 0$, horizontal grid), respectively [22].

### *B. Measured Scattering Vectors*

Substituting the signature matrices of the various calibrators into the CTLR mode system model (3) and neglecting the noise terms gives the following measured scattering vectors for the different calibrators, where the superscript denotes the type of calibrator:

$$\begin{bmatrix} M_{RH}^{Tri} \\ M_{RV}^{Tri} \end{bmatrix} = \begin{bmatrix} e^{-2j\Omega} + \delta_c e^{2j\Omega} - j\delta_2 e^{-2j\Omega} + j\delta_2\delta_c e^{2j\Omega} \\ \delta_1 e^{-2j\Omega} + \delta_1\delta_c e^{2j\Omega} - jfe^{-2j\Omega} + jf\delta_c e^{2j\Omega} \end{bmatrix} \tag{9}$$

$$\begin{bmatrix} M_{RH}^{Di} \\ M_{RV}^{Di} \end{bmatrix} = \begin{bmatrix} 1 + \delta_c + j\delta_2 - j\delta_2\delta_c \\ \delta_1 + \delta_1\delta_c + jf - jf\delta_c \end{bmatrix} \tag{10}$$

$$\begin{bmatrix} M_{RH}^{Gt1} \\ M_{RV}^{Gt1} \end{bmatrix} = \frac{1}{2}\begin{bmatrix} 1 + e^{-2j\Omega} + j\delta_2 - j\delta_2 e^{-2j\Omega} + \delta_c e^{2j\Omega} + \delta_c + j\delta_2\delta_c e^{2j\Omega} - j\delta_2\delta_c \\ \delta_1 + \delta_1 e^{-2j\Omega} + jf - jfe^{-2j\Omega} + \delta_1\delta_c e^{2j\Omega} + \delta_1\delta_c + jf\delta_c e^{2j\Omega} - jf\delta_c \end{bmatrix} \tag{11}$$

$$\begin{bmatrix} M_{RH}^{Gt2} \\ M_{RV}^{Gt2} \end{bmatrix} = \frac{1}{2}\begin{bmatrix} -1 + e^{-2j\Omega} - j\delta_2 - j\delta_2 e^{-2j\Omega} + \delta_c e^{2j\Omega} - \delta_c + j\delta_2\delta_c e^{2j\Omega} + j\delta_2\delta_c \\ -\delta_1 + \delta_1 e^{-2j\Omega} - jf - jfe^{-2j\Omega} + \delta_1\delta_c e^{2j\Omega} - \delta_1\delta_c + jf\delta_c e^{2j\Omega} + jf\delta_c \end{bmatrix} \tag{12}$$

$$\begin{bmatrix} M_{RH}^{X} \\ M_{RV}^{X} \end{bmatrix} = \frac{1}{2}\begin{bmatrix} -j + je^{-2j\Omega} + \delta_2 + \delta_2 e^{-2j\Omega} - j\delta_c e^{2j\Omega} + j\delta_c + \delta_2\delta_c e^{2j\Omega} + \delta_2\delta_c \\ -j\delta_1 + j\delta_1 e^{-2j\Omega} + f + fe^{-2j\Omega} + f\delta_c e^{2j\Omega} + f\delta_c - j\delta_1\delta_c e^{2j\Omega} + j\delta_1\delta_c \end{bmatrix} \tag{13}$$

$$\begin{bmatrix} M_{RH}^{Y} \\ M_{RV}^{Y} \end{bmatrix} = \frac{1}{2}\begin{bmatrix} -j - je^{-2j\Omega} + \delta_2 - \delta_2 e^{-2j\Omega} + j\delta_c e^{2j\Omega} + j\delta_c - \delta_2\delta_c e^{2j\Omega} + \delta_2\delta_c \\ -j\delta_1 - j\delta_1 e^{-2j\Omega} + f - fe^{-2j\Omega} - f\delta_c e^{2j\Omega} + f\delta_c + j\delta_1\delta_c e^{2j\Omega} + j\delta_1\delta_c \end{bmatrix} \tag{14}$$

$$\begin{bmatrix} M_{RH}^{P} \\ M_{RV}^{P} \end{bmatrix} = \begin{bmatrix} 1 + \delta_c - je^{-2j\Omega} + j\delta_c e^{2j\Omega} - \delta_2 e^{-2j\Omega} - \delta_2\delta_c e^{2j\Omega} + j\delta_2 - j\delta_2\delta_c \\ \delta_1 + \delta_1\delta_c - j\delta_1 e^{-2j\Omega} + j\delta_1\delta_c e^{2j\Omega} - fe^{-2j\Omega} - f\delta_c e^{2j\Omega} + jf - jf\delta_c \end{bmatrix} \tag{15}$$

### *C. Combination of Mixed Calibrators*

From (4) and (8), the following relationships between the measurements from the different calibrators can be easily derived:

$$M_{RH}^{Gt1} - M_{RH}^{Gt2} = M_{RH}^{Di}$$

$$M_{RV}^{Gt1} - M_{RV}^{Gt2} = M_{RV}^{Di}$$

$$M_{RH}^{Gt1} + M_{RH}^{Gt2} = M_{RH}^{Tri}$$

$$M_{RV}^{Gt1} + M_{RV}^{Gt2} = M_{RV}^{Tri}$$

$$M_{RH}^{X} - M_{RH}^{Y} = M_{RH}^{Di} - M_{RH}^{P}$$

$$M_{RV}^{X} - M_{RV}^{Y} = M_{RV}^{Di} - M_{RV}^{P} \tag{16}$$

Equation (16) indicates that a combination of Gt1 and Gt2 could replace the trihedral and dihedral, and a $PARC_P$ could be replaced by a combination of a $PARC_X$, a $PARC_Y$ and a dihedral.

If we restrict the number of calibration devices to at most four, we have the following six schemes for calibrating the CTLR mode:

(1) Trihedral + Dihedral + $PARC_P$;

(2) Dihedral + $PARC_X$ +$PARC_Y$;

(3) Trihedral + $PARC_X$ +$PARC_Y$;

(4) Gt1 + Gt2 + $PARC_P$;

(5) Gt1 + Gt2 + $PARC_X$ + $PARC_Y$;

(6) Trihedral + Dihedral + $PARC_X$ + $PARC_Y$.

It can be seen from (16) that scheme (4) is equivalent to scheme (1), while schemes (5) and (6) are equivalent to the combination of schemes (1) and (2). Schemes (1) - (4) employ fewer calibrators than schemes (5) and (6), so would appear preferable in terms of economy and complexity. However, schemes (5) and (6) can exploit redundancy to improve the precision of estimating both the FR and the radar system error terms (see Part E, Section III).

*D. Algorithms for Calibrating Compact Polarization SAR*

From (9)-(15), we can derive

$$\begin{aligned}
M_{RH}^{X} + M_{RH}^{Y} &= -jM_{RH}^{Di} + 2j\delta_c + 2\delta_2\delta_c \\
M_{RV}^{X} + M_{RV}^{Y} &= -jM_{RV}^{Di} + 2f\delta_c + 2j\delta_1\delta_c \\
M_{RH}^{Di} - M_{RH}^{P} &= jM_{RH}^{Tri} - 2j\delta_c e^{2j\Omega} + 2\delta_2\delta_c e^{2j\Omega} \\
M_{RV}^{Di} - M_{RV}^{P} &= jM_{RV}^{Tri} + 2f\delta_c e^{2j\Omega} - 2j\delta_1\delta_c e^{2j\Omega} \\
M_{RH}^{X} - M_{RH}^{Y} &= jM_{RH}^{Tri} - 2j\delta_c e^{2j\Omega} + 2\delta_2\delta_c e^{2j\Omega} \\
M_{RV}^{X} - M_{RV}^{Y} &= jM_{RV}^{Tri} + 2f\delta_c e^{2j\Omega} - 2j\delta_1\delta_c e^{2j\Omega}
\end{aligned} \tag{17}$$

Neglecting the second order small values (i.e. terms of the form $\delta_2\delta_c$, $\delta_1\delta_c$, etc.), an estimate of

channel imbalance *f*, denoted as $\hat{f}$, can be derived from (17). This can then be used to derive an estimate of the L-R circular cross-talk $\delta_c$, represented as $\hat{\delta}_c$. Finally, $\hat{f}$ and $\hat{\delta}_c$ are treated as known values and used to derive the cross-talk terms, $\delta_1$ and $\delta_2$, and the FR, $\Omega$.

Following such a procedure, the calibration algorithms for schemes (1)-(6) can be derived from (16) and (17), and expressed as:

**Scheme 1.**

$$\begin{aligned}
\hat{f}^{(1)} &= \frac{M_{RV}^{Di} - M_{RV}^{P} - jM_{RV}^{Tri}}{M_{RH}^{Tri} + j\left(M_{RH}^{Di} - M_{RH}^{P}\right)} \\
\hat{\delta}_c^{(1)} &= \frac{\left(M_{RH}^{Di} - M_{RH}^{P} - jM_{RH}^{Tri}\right)\cdot\left(j\hat{f}^{(1)}M_{RH}^{Tri} - M_{RV}^{Tri}\right)}{4\hat{f}^{(1)}} \\
\hat{\delta}_1^{(1)} &= \frac{M_{RV}^{Di} + j\left(\hat{\delta}_c^{(1)} - \hat{f}^{(1)}\right)}{1+\hat{\delta}_c^{(1)}} \\
\hat{\delta}_2^{(1)} &= \frac{j\left(1+\hat{\delta}_c^{(1)} - M_{RH}^{Di}\right)}{1-\hat{\delta}_c^{(1)}} \\
\hat{\Omega}^{(1)} &= \frac{1}{2}\arg\left\{\frac{2\hat{f}^{(1)}}{\hat{f}^{(1)}\cdot M_{RH}^{Tri} + j\cdot M_{RV}^{Tri}}\right\}
\end{aligned} \tag{18}$$

**Scheme 2.**

$$\begin{aligned}
\hat{f}^{(2)} &= \frac{M_{RV}^{X} + M_{RV}^{Y} + jM_{RV}^{Di}}{M_{RH}^{Di} - j\left(M_{RH}^{X} + M_{RH}^{Y}\right)} \\
\hat{\delta}_c^{(2)} &= \frac{1}{2}\left[M_{RH}^{Di} - j\left(M_{RH}^{X} + M_{RH}^{Y}\right)\right] \\
\hat{\delta}_1^{(2)} &= \frac{1}{2}\left[M_{RV}^{Di} + j\left(M_{RV}^{X} + M_{RV}^{Y}\right)\right] - j\hat{f}^{(2)} \\
\hat{\delta}_2^{(2)} &= \frac{1}{2}\left[M_{RH}^{X} + M_{RH}^{Y} - jM_{RH}^{Di}\right] + j \\
\hat{\Omega}^{(2)} &= \frac{1}{2}\arg\left\{\frac{\left(j\hat{\delta}_1^{(2)} + \hat{f}^{(2)}\right)\cdot\left(M_{RH}^{X} - M_{RH}^{Y}\right) - \left(j+\hat{\delta}_2^{(2)}\right)\cdot\left(M_{RV}^{X} - M_{RV}^{Y}\right)}{\left(\hat{\delta}_2^{(2)}\hat{\delta}_c^{(2)} - j\hat{\delta}_c^{(2)}\right)\left(j\hat{\delta}_1^{(2)} + \hat{f}^{(2)}\right) - \left(\hat{f}\hat{\delta}_c^{(2)} - j\hat{\delta}_2^{(2)}\hat{\delta}_c^{(2)}\right)\left(j+\hat{\delta}_2^{(2)}\right)}\right\}
\end{aligned} \tag{19}$$

**Scheme 3.**

$$\begin{aligned}
\hat{f}^{(3)} &= \frac{M_{RV}^{X} - M_{RV}^{Y} - jM_{RV}^{Tri}}{M_{RH}^{Tri} + j\left(M_{RH}^{X} - M_{RH}^{Y}\right)} \equiv \hat{f}^{(1)} \\
\hat{\delta}_c^{(3)} &= \frac{\left(M_{RH}^{X} - M_{RH}^{Y} - jM_{RH}^{Tri}\right)\cdot\left(j\hat{f}^{(3)}M_{RH}^{Tri} - M_{RV}^{Tri}\right)}{4\hat{f}^{(3)}} \equiv \hat{\delta}_c^{(1)} \\
\hat{\delta}_1^{(3)} &= \frac{-j\hat{f}^{(3)}\left(M_{RV}^{X} - M_{RV}^{Y} + jM_{RV}^{Tri}\right)}{\hat{f}^{(3)}\cdot M_{RH}^{Tri} + j\cdot M_{RV}^{Tri}} + j\hat{f}^{(3)} \\
\hat{\delta}_2^{(3)} &= \frac{\hat{f}^{(3)}\left(M_{RH}^{X} - M_{RH}^{Y} + jM_{RH}^{Tri}\right)}{\hat{f}^{(3)}\cdot M_{RH}^{Tri} + j\cdot M_{RV}^{Tri}} - j
\end{aligned}$$

$$\hat{\Omega}^{(3)} = \frac{1}{2}\arg\left\{\frac{2\hat{f}^{(3)}}{\hat{f}^{(3)}\cdot M_{RH}^{Tri} + j\cdot M_{RV}^{Tri}}\right\} \equiv \hat{\Omega}^{(1)} \tag{20}$$

**Scheme 4.**

Since the trihedral and dihedral can be replaced by the combination of Gt1 and Gt2, scheme 4 is equivalent to scheme 1, and yields:

$$\hat{f}^{(4)} = \frac{\left(M_{RV}^{Gt1} - M_{RV}^{Gt2}\right) - M_{RV}^{P} - j\left(M_{RV}^{Gt1} + M_{RV}^{Gt2}\right)}{\left(M_{RH}^{Gt1} + M_{RH}^{Gt2}\right) + j\left[\left(M_{RH}^{Gt1} - M_{RH}^{Gt2}\right) - M_{RH}^{P}\right]} \equiv \hat{f}^{(1)}$$

$$\hat{\delta}_c^{(4)} = \frac{\left(M_{RV}^{Gt1} - M_{RV}^{Gt2}\right) - M_{RV}^{P} - j\left(M_{RV}^{Gt1} + M_{RV}^{Gt2}\right)}{4\hat{f}^{(4)}} \times \left[j\hat{f}^{(4)}\left(M_{RH}^{Gt1} + M_{RH}^{Gt2}\right) - \left(M_{RV}^{Gt1} + M_{RV}^{Gt2}\right)\right] \equiv \hat{\delta}_c^{(1)}$$

$$\hat{\delta}_1^{(4)} = \frac{\left(M_{RV}^{Gt1} - M_{RV}^{Gt2}\right) + j\left(\hat{\delta}_c^{(4)} - \hat{f}^{(4)}\right)}{1 + \hat{\delta}_c^{(4)}} \equiv \hat{\delta}_1^{(1)}$$

$$\hat{\delta}_2^{(4)} = \frac{j\left[1 + \hat{\delta}_c^{(4)} - \left(M_{RH}^{Gt1} - M_{RH}^{Gt2}\right)\right]}{1 - \hat{\delta}_c^{(4)}} \equiv \hat{\delta}_2^{(1)}$$

$$\hat{\Omega}^{(4)} = \frac{1}{2}\arg\left\{\frac{2\hat{f}^{(4)}}{\hat{f}^{(4)}\cdot\left(M_{RH}^{Gt1} + M_{RH}^{Gt2}\right) + j\cdot\left(M_{RV}^{Gt1} + M_{RV}^{Gt2}\right)}\right\} \equiv \hat{\Omega}^{(1)} \tag{21}$$

**Scheme 5.**

From (16), scheme 5 is equivalent to the combination of schemes 1 and 2, resulting in two alternative estimates for the channel imbalance, *f*, and the L-R circular cross-talk, $\delta_c$, giving:

$$\hat{f}^{(5A)} = \frac{M_{RV}^{X} + M_{RV}^{Y} + j\left(M_{RV}^{Gt1} - M_{RV}^{Gt2}\right)}{\left(M_{RH}^{Gt1} - M_{RH}^{Gt2}\right) - j\left(M_{RH}^{X} + M_{RH}^{Y}\right)} \equiv \hat{f}^{(1)}, \text{ or}$$

$$\hat{f}^{(5B)} = \frac{M_{RV}^{X} - M_{RV}^{Y} - j\left(M_{RV}^{Gt1} + M_{RV}^{Gt2}\right)}{\left(M_{RH}^{Gt1} + M_{RH}^{Gt2}\right) + j\left(M_{RH}^{X} - M_{RH}^{Y}\right)} \equiv \hat{f}^{(2)}$$

$$\hat{\delta}_c^{(5A)} = \frac{\left[M_{RH}^{X} - M_{RH}^{Y} - j(M_{RH}^{Gt1} + M_{RH}^{Gt2})\right]}{4\hat{f}^{(5)}} \times \left[j\hat{f}^{(5)}(M_{RH}^{Gt1} + M_{RH}^{Gt2}) - (M_{RV}^{Gt1} + M_{RV}^{Gt2})\right] \equiv \hat{\delta}_c^{(1)}, \text{ or}$$

$$\hat{\delta}_c^{(5B)} = \frac{1}{2}\left[\left(M_{RH}^{Gt1} - M_{RH}^{Gt2}\right) - j\left(M_{RH}^{X} + M_{RH}^{Y}\right)\right] \equiv \hat{\delta}_c^{(2)}$$

$$\hat{\delta}_1^{(5)} = \frac{1}{2}\left[M_{RV}^{Gt1} - M_{RV}^{Gt2} + j\left(M_{RV}^{X} + M_{RV}^{Y}\right)\right] - j\hat{f}^{(5)} \cong \hat{\delta}_1^{(2)}$$

$$\hat{\delta}_2^{(5)} = \frac{1}{2}\left[M_{RH}^{X} + M_{RH}^{Y} - j\left(M_{RH}^{Gt1} - M_{RH}^{Gt2}\right)\right] + j \equiv \hat{\delta}_2^{(2)}$$

$$\hat{\Omega}^{(5)} = \frac{1}{2}\arg\left\{\frac{2\hat{f}^{(5)}}{\hat{f}^{(5)}\cdot\left(M_{RH}^{Gt1} + M_{RH}^{Gt2}\right) + j\cdot\left(M_{RV}^{Gt1} + M_{RV}^{Gt2}\right)}\right\} \cong \hat{\Omega}^{(1)} \tag{22}$$

**Scheme 6.**

From (16), scheme 6 is seen to be equivalent to scheme 5, and therefore also has two alternative estimates for *f* and $\delta_c$:

$$\hat{f}^{(6A)} = \frac{M_{RV}^{X} + M_{RV}^{Y} + jM_{RV}^{Di}}{M_{RH}^{Di} - j\left(M_{RH}^{X} + M_{RH}^{Y}\right)} \equiv \hat{f}^{(1)}, \text{ or}$$

$$\hat{f}^{(6B)} = \frac{M_{RV}^{X} - M_{RV}^{Y} - jM_{RV}^{Tri}}{M_{RH}^{Tri} + j\left(M_{RH}^{X} - M_{RH}^{Y}\right)} \equiv \hat{f}^{(2)}$$

$$\hat{\delta}_c^{(6A)} = \hat{\delta}_c^{(1)}, \text{ or}$$

$$\hat{\delta}_c^{(6B)} = \hat{\delta}_c^{(2)}$$

$$\hat{\delta}_1^{(6)} = \frac{1}{2}\left[M_{RV}^{Di} + j\left(M_{RV}^{X} + M_{RV}^{Y}\right)\right] - j\hat{f}^{(6)} \cong \hat{\delta}_1^{(2)}$$

$$\hat{\delta}_2^{(6)} = \frac{1}{2}\left[M_{RH}^{X} + M_{RH}^{Y} - jM_{RH}^{Di}\right] + j \equiv \hat{\delta}_2^{(2)}$$

$$\hat{\Omega}^{(6)} = \frac{1}{2}\arg\left\{\frac{2\hat{f}^{(6)}}{\hat{f}^{(6)} \cdot M_{RH}^{Tri} + j \cdot M_{RV}^{Tri}}\right\} \cong \hat{\Omega}^{(1)} \tag{23}$$

The use of the symbol "$\cong$" in the expressions for $\delta_1$ and $\Omega$ in schemes 5 and 6 is because they depend on which of the two estimates of $f$ are used. In practice, this distinction fades away, as an optimized value of $f$ that combines these two estimates is used in the final calibration scheme (see section III. E).

*E. Analysis and Optimization*

Equations (18) - (23) present the detailed algorithms for calibrating CTLR mode SAR with six sets of mixed calibrators. It is evident that the estimates of $f$ and $\delta_c$ are key factors in the calibration algorithms, since they are utilized to derive the estimates of $\delta_1$, $\delta_2$ and $\Omega$. In particular, accurate estimation of the channel imbalance, $f$, is extremely important.

Using (17), one can derive the relations between the true channel imbalance, $f$, and its two estimates, $f^{(1)}$ and $f^{(2)}$, in the form:

$$f = \frac{\left(M_{RV}^{Di} - M_{RV}^{P} - jM_{RV}^{Tri}\right) + 2j\delta_1\delta_c e^{2j\Omega}}{\left[M_{RH}^{Tri} + j\left(M_{RH}^{Di} - M_{RH}^{P}\right)\right] - 2j\delta_2\delta_c e^{2j\Omega}} \approx \hat{f}^{(1)} \cdot \left(1 + \Delta_1\right)$$

$$f = \frac{\left(M_{RV}^{X} + M_{RV}^{Y} + jM_{RV}^{Di}\right) - 2j\delta_1\delta_c}{\left[M_{RH}^{Di} - j\left(M_{RH}^{X} + M_{RH}^{Y}\right)\right] + 2j\delta_2\delta_c} \approx \hat{f}^{(2)} \cdot \left(1 - \Delta_2\right) \tag{24}$$

where

$$\Delta_1 = \frac{2j\delta_c\left(\delta_1 B_1 + \delta_2 A_1\right)e^{2j\Omega}}{A_1 \cdot B_1} \equiv \frac{j\left(\delta_1 + f\delta_2\right)}{\left(f + \delta_1\delta_2\right) + j\left(f\delta_2 - \delta_1\right)}$$

$$\Delta_2 = \frac{2j\delta_c(\delta_1 B_2 + \delta_2 A_2)}{A_2 \cdot B_2} \equiv \frac{j(\delta_1 + f\delta_2)}{(f + \delta_1\delta_2) - j(f\delta_2 - \delta_1)}$$

$$A_1 = M_{RV}^{Di} - M_{RV}^{P} - jM_{RV}^{Tri} \equiv 2\delta_c(f - j\delta_1)e^{2j\Omega}$$

$$B_1 = M_{RH}^{Tri} + j(M_{RH}^{Di} - M_{RH}^{P}) \equiv 2\delta_c(1 + j\delta_2)e^{2j\Omega}$$

$$A_2 = M_{RV}^{X} + M_{RV}^{Y} + jM_{RV}^{Di} \equiv 2\delta_c(f + j\delta_1)$$

$$B_2 = M_{RH}^{Di} - j(M_{RH}^{X} + M_{RH}^{Y}) \equiv 2\delta_c(1 - j\delta_2)$$

with $f^{(1)} = A_1 / B_1$, $f^{(2)} = A_2 / B_2$ and $|\Delta_1| \cong |\Delta_2|$.

Because $|\Delta_1| << 1$ and $|\Delta_2| << 1$, they should not significantly affect the estimate of amplitude imbalance, $|f|$, but they will lead to biased estimates of the phase imbalance $\arg\{f\}$, resulting in errors when estimating $\delta_c$ and $\Omega$. From (24), it is seen that the phase error in the estimate $\hat{f}^{(1)}$ has a bias of opposite sign to that in $\hat{f}^{(2)}$, so a better estimate of the phase is given by $\arg\left(\hat{f}^{(1)} \cdot \hat{f}^{(2)}\right)/2$. The optimised estimate of channel imbalance, $\hat{f}$, therefore takes this value as its argument and $\sqrt{\left|\hat{f}^{(1)} \cdot \hat{f}^{(2)}\right|}$ as its amplitude.

Similarly, from (17) it can be seen that the relations between $\delta_c$ and its two estimates, $\delta_c^{(1)}$ and $\delta_c^{(2)}$, are given by

$$\delta_c = \frac{B_1 \cdot e^{-2j\Omega}}{2(1 + j\delta_2)} \approx \hat{\delta}_c^{(1)} \cdot (1 - j\delta_2)$$

$$\delta_c = \frac{B_2}{2(1 - j\delta_2)} \approx \hat{\delta}_c^{(2)} \cdot (1 + j\delta_2) \qquad (25)$$

It is clear that the biases in the phases of $\hat{\delta}_c^{(1)}$ and $\hat{\delta}_c^{(2)}$ are of opposite sign, so that $\arg\left(\hat{\delta}_c^{(1)} \cdot \hat{\delta}_c^{(2)}\right)/2$ is an optimized phase estimate for $\delta_c$. However, since $\hat{\delta}_c^{(1)}$ depends on $\hat{f}^{(1)}$, $\left|\hat{\delta}_c^{(2)}\right|$ is preferred as the amplitude estimate for $\delta_c$.

A major advantage of schemes 5 and 6 is that they are the only schemes providing two alternative estimates for $f$ and $\delta_c$, which can be used as above to improve the accuracy of the estimates. This suggests the use of these schemes as the preferred calibration scenarios.

Both $\delta_1$ and $\delta_2$, have three different estimates, provided by schemes 1-3, respectively. Of these, $\hat{\delta}_1^{(1)}$ and $\hat{\delta}_2^{(1)}$ might be expected to be the most accurate, since they are derived directly by solving (10), without neglecting any small values. However, their dependence on the estimation accuracy of $f$ and $\delta_c$ tends to cause larger errors (see Figs. 6-9). In contrast, many small values are ignored in deriving $\hat{\delta}_1^{(3)}$ and $\hat{\delta}_2^{(3)}$, reducing their accuracy (see Figs. 6-9). Scheme 2 is therefore the preferred approach for estimating $\delta_1$ and $\delta_2$, and is further improved by replacing $\hat{f}^{(2)}$ with the optimized estimate $\hat{f}$. For the same reason, the optimal FR estimate takes the form of scheme 1 with $\hat{f}^{(1)}$ replaced by the optimized estimate of $f$. In practice, we use the equivalent expressions for $\delta_1$, $\delta_2$ and $\Omega$ from schemes 5 or 6. These optimizations are validated by the numerical simulations presented in Part B, Section IV.

Hence, for scheme 5, the optimized calibration algorithm is:

$$\hat{f} = \left|\hat{f}^{(5A)} \cdot \hat{f}^{(5B)}\right|^{\frac{1}{2}} \cdot \exp\left\{j \cdot \frac{\arg(\hat{f}^{(5A)} \cdot \hat{f}^{(5B)})}{2}\right\}$$

$$\hat{\delta}_c = \left|\hat{\delta}_c^{(5B)}\right| \cdot \exp\left\{j \frac{\arg(\hat{\delta}_c^{(5A)} \cdot \hat{\delta}_c^{(5B)})}{2}\right\}$$

$$\hat{\delta}_1 = \frac{1}{2}\left[M_{RV}^{Gt1} - M_{RV}^{Gt2} + j\left(M_{RV}^{X} + M_{RV}^{Y}\right)\right] - j\hat{f}$$

$$\hat{\delta}_2 = \frac{1}{2}\left[M_{RH}^{X} + M_{RH}^{Y} - j\left(M_{RH}^{Gt1} - M_{RH}^{Gt2}\right)\right] + j$$

$$\hat{\Omega} = \frac{1}{2}\arg\left\{\frac{2\hat{f}}{\hat{f} \cdot \left(M_{RH}^{Gt1} + M_{RH}^{Gt2}\right) + j \cdot \left(M_{RV}^{Gt1} + M_{RV}^{Gt2}\right)}\right\} \tag{26}$$

Similarly, the optimized calibration algorithm for scheme 6 is:

$$\hat{f} = \left|\hat{f}^{(6A)} \cdot \hat{f}^{(6B)}\right|^{\frac{1}{2}} \cdot \exp\left\{j \cdot \frac{\arg(\hat{f}^{(6A)} \cdot \hat{f}^{(6B)})}{2}\right\}$$

$$\hat{\delta}_c = \left|\hat{\delta}_c^{(6B)}\right| \cdot \exp\left\{j \cdot \frac{\arg(\hat{\delta}_c^{(6A)} \cdot \hat{\delta}_c^{(6B)})}{2}\right\}$$

$$\hat{\delta}_1 = \frac{1}{2}\left[M_{RV}^{Di} + j\left(M_{RV}^{X} + M_{RV}^{Y}\right)\right] - j\hat{f}$$

$$\hat{\delta}_2 = \frac{1}{2}\left[M_{RH}^{X} + M_{RH}^{Y} - jM_{RH}^{Di}\right] + j$$

$$\hat{\Omega} = \frac{1}{2}\arg\left\{\frac{2\hat{f}}{\hat{f}\cdot M_{RH}^{Tri} + j\cdot M_{RV}^{Tri}}\right\} \tag{27}$$

Note that (16) implies that (26) is equivalent to (27) if issues of calibrator performance are ignored. However, gridded trihedrals, as used in Scheme 5 have the advantages of providing large beamwidth and giving average polarimetric noise (i.e., the coherent averaging of scattering vectors from different angular positions) less than -30 dB [22]. On the negative side, they require accurate construction of the grid, and the microwave absorber layer is likely to be affected by rain. In contrast, scheme 6's use of a trihedral and dihedral instead of gridded trihedrals brings the merits of simple construction and little effect from rain, but the narrow beamwidth of the dihedral causes orientation difficulties, and the dihedral suffers from high polarimetric noise due to pointing error [22].

*F. Correcting FR Estimation Ambiguity Using TEC Data*

The optimized FR estimates in (26) and (27) lie between $\pm\pi/2$, leading to an ambiguity of $\pm k\pi$. However, this can be removed by using (1) to provide an independent estimate of FR, where TEC is given by the global ionospheric TEC maps estimated by the Global Navigation Satellite System (GNSS) and use is made of the IGRF10 model for the Earth's magnetic field [4]. The International GNSS Service provides bi-hourly global TEC maps with grid-points spaced $5^o$ in longitude and $2.5^o$ in latitude [4], [23], with an overall root mean square (RMS) error of 3-5 TECU [23] and [24]. This corresponds to an FR error that increases with latitude (see (19) in [25]) and has the value 18.3° at 80° latitude for a P-band SAR (see Table I in [25]). Hence an unambiguous FR estimator is given by [25]:

$$\hat{\Omega}^F = \hat{\Omega} + \text{round}\left(\frac{\hat{\Omega}_{GNSS} - \hat{\Omega}}{\pi/2}\right)\cdot\frac{\pi}{2} \tag{28}$$

where round{·} denotes rounding to the nearest integer, $\hat{\Omega}_{GNSS}$ is the FR predicted from GNSS TEC data and $\hat{\Omega}$ is taken from (18)-(23), (26) and (27). This expression would only lead to incorrect estimates if the error in $\hat{\Omega}_{GNSS}$ exceeded 45°, i.e., even at the highest latitudes, errors in TEC exceeding 2.5 times the expected RMS error.

## IV. Simulation Results And Discussion

### A. Simulation Parameters

Numerical simulations were carried out to assess the proposed methods. The measured backscattering matrices were derived from (3), under given conditions of FR, channel imbalance and cross-talk. In order to test the proposed calibration algorithms fully, the error terms in (3) were allowed to have wide variation: in the simulations, FR ranged from 0° to 360°, amplitude imbalance was taken to be less than 3 dB, the amplitude of the linear cross-talk terms varied over the range -40 dB to -20 dB, the L-R circular cross-talk, $\delta_c$, ranged from -30 dB to -10 dB, and the arguments of both phase imbalance and the cross-talk terms were taken to lie within ±60°.

The impact of GNSS TEC errors on FR estimation performance was simulated by assuming an unbiased Gaussian TEC error with standard deviation (SD) 5 TECU, which corresponds to an FR error with SD 13° at latitude 40° (see Table 1 in [25]).

In the set of simulations presented in Part B, Section IV, only radar system impacts are considered, while Part C deals with the simulation and evaluation of calibrator errors on calibration accuracy. Note that in these simulations the data were corrupted with the maximum values of the radar system errors, i.e. $|f| = 1.5$ (3.5 dB), $\arg\{f\} = \pi/3$ (60°) and $|\delta_1| = |\delta_2| = 0.1$ (-20 dB), $|\delta_c| = 0.32$ (-10 dB), in order to test the proposed algorithms severely.

### B. Simulation of Calibration Performance

From (18)-(23), (26) and (27), it is apparent that there are three different estimates for $f$, $\delta_c$, $\delta_2$ and $\Omega$, namely $\hat{f}^{(1)}$, $\hat{f}^{(2)}$ and $\hat{f}$; $\hat{\delta}_c^{(1)}$, $\hat{\delta}_c^{(2)}$ and $\hat{\delta}_c$; $\hat{\delta}_2^{(1)}$, $\hat{\delta}_2^{(3)}$ and $\hat{\delta}_2$; $\hat{\Omega}^{(1)}$, $\hat{\Omega}^{(2)}$ and $\hat{\Omega}$, respectively, and four estimates for $\delta_1$ (i.e. $\hat{\delta}_1^{(1)}$, $\hat{\delta}_1^{(2)}$, $\hat{\delta}_1^{(3)}$ and $\hat{\delta}_1$). Note that $\hat{f}$, $\hat{\delta}_c$, $\hat{\delta}_1$, $\hat{\delta}_2$ and $\hat{\Omega}$ are the optimal estimates provided by (26) or (27), whose superior performance is demonstrated by the simulation results shown in Figs. 2-10 (curves with superscript “Optimal”).

Figs. 2 and 3 illustrate the near-perfect performance of $\hat{f}$ in estimating amplitude and phase

imbalance, respectively. Similarly, Figs. 4 and 5 demonstrate the excellent performance of $\hat{\delta}_c$ as an estimator of both the amplitude and phase of $\delta_c$. Figs. 3 and 5 also confirm that the phase estimates of $\hat{f}^{(1)}$ and $\hat{\delta}_c^{(1)}$ are oppositely biased to those of $\hat{f}^{(2)}$ and $\hat{\delta}_c^{(2)}$, as expected from the theoretical analysis in (24) and (25).

Figs. 6-9 show that $\hat{\delta}_1$ and $\hat{\delta}_2$ provide the best estimates of the amplitude and phase of $\delta_1$ and $\delta_2$. The curves labeled "Original" denote the estimates derived from (18)-(20), while those labeled "Modified" correspond to estimates where $\hat{f}$ is substituted for $\hat{f}^{(1)}$ and $\hat{f}^{(2)}$ in (18) and (19), and $\hat{\delta}_c$ is substituted for $\hat{\delta}_c^{(1)}$ in (18). It can be seen that the original estimates for $\delta_1$ and $\delta_2$ perform less well than the modified estimates due to errors in the estimates of $f$ and $\delta_c$ derived in schemes 1-3. In particular, the modified $\hat{\delta}_1^{(1)}$ provides nearly identical accuracy to $\hat{\delta}_1$, and $\hat{\delta}_2^{(1)}$ gives comparable accuracy to $\hat{\delta}_2$ (see curves marked with "x" in Figs. 6-9). This indicates that $\hat{\delta}_1^{(1)}$ and $\hat{\delta}_2^{(1)}$ would perform well if they employed the more accurate estimates $\hat{f}$ and $\hat{\delta}_c$, because second order terms are not neglected in their derivation. This is consistent with the theoretical analysis presented in Part E, Section III.

Fig. 10 demonstrates how the estimated FR error changes with respect to true FR, under different initial phase imbalances of 0° and 60°. Note that the modified $\hat{\Omega}^{(2)}$ here is derived by substituting the optimal estimates $\hat{f}$, $\hat{\delta}_c$, $\hat{\delta}_1$ and $\hat{\delta}_2$ into (19). It can be seen that the FR estimates are biased due to radar system errors. However, the optimal FR estimate from scheme 5 or 6 provides the best performance, validating the effectiveness of the proposed FR estimation method (see Table II).

Table I presents a statistical analysis of the amplitude and phase errors corresponding to the optimal channel imbalance and cross-talk estimates in Figs. 2-9. It shows that $\hat{\delta}_2$ and $\hat{f}$ have nearly perfect performance, $\hat{\delta}_c$ shows a phase bias of 1.2°, while $\hat{\delta}_1$ has an amplitude bias of -2.5 dB and phase bias of 1.0°. The statistical analysis of the estimated FR errors corresponding to Fig. 10 is shown in Table II; this indicates that $\hat{\Omega}$ is the FR estimator with the best performance, with maximum mean FR

error (i.e. FR bias) of 0.9°. This indicates that $\delta_c$ needs to be smaller than approximately -10 dB if FR bias is not to exceed 1°.

*C. Average Polarimetric Noise Evaluation*

If the calibrators are perfectly constructed, then (16) and (17) indicate that schemes 5 and 6 are mathematically equivalent, and Figs. 2-10 demonstrate the equally excellent performance of optimal calibration algorithms based on these schemes. However, the calibrators may contain errors in their polarimetric characteristics, due to imperfect construction, inaccurate orientation, etc. These errors can be referred to as average polarimetric noise (APN), which may have significant impacts on calibration accuracy. The influence of APN on the two optimal calibration schemes 5 and 6 can be evaluated by means of numerical simulation [19].

For scheme 5, the error models of the calibration targets are given by [19]

$$\mathbf{S}'_{Gt1}=\begin{bmatrix}1 & \delta\\ \delta & \delta^2\end{bmatrix},\ \mathbf{S}'_{Gt2}=\begin{bmatrix}\delta^2 & \delta\\ \delta & 1\end{bmatrix},\ \mathbf{S}'_{X}=\begin{bmatrix}\delta & \delta^2\\ 1 & \delta\end{bmatrix},\ \mathbf{S}'_{Y}=\begin{bmatrix}\delta & 1\\ \delta^2 & \delta\end{bmatrix}$$

and for scheme 6 by [18]

$$\mathbf{S}'_{Tri}=\begin{bmatrix}1 & \delta\\ \delta & 1+\delta^2\end{bmatrix},\ \mathbf{S}'_{Di}=\begin{bmatrix}1 & \delta_{Di}\\ \delta_{Di} & -1+\delta_{Di}^2\end{bmatrix},\ \mathbf{S}'_{X}=\begin{bmatrix}\delta & \delta^2\\ 1 & \delta\end{bmatrix},\ \mathbf{S}'_{Y}=\begin{bmatrix}\delta & 1\\ \delta^2 & \delta\end{bmatrix}$$

where we have used the same notation as in (4)-(6). For simplicity, we here assume that the APNs of the Gt1, Gt2, $\mathrm{PARC_X}$, $\mathrm{PARC_Y}$ and trihedral calibrators are the same, with complex value, $\delta$, while the APN for the dihedral is larger [22]. To derive the simulation results in Figs. 11-13 we have assumed $\delta_{Di}=\sqrt{10}\,\delta$, so that the dihedral has an APN 10 dB larger than the other calibrators.

Figs. 11 and 12 compare the amplitude and phase errors of the estimated channel imbalance and cross-talks derived from schemes 5 and 6 as a function of APN amplitude and phase, respectively, while Fig. 13 shows the associated FR errors. Here, the APN amplitude is varied over the range -60 dB to -30 dB, and the APN phase lies within ±60°. Fig. 11 indicates that APN with amplitude -40 dB does not lead to a large amplitude estimation error. Thus we assume $|\delta|$ = -40 dB in evaluating the APN phase error in Figs. 12 and 13(b). Figs. 11-13 show that, although schemes 5 and 6 are mathematically

identical, scheme 5 has much better tolerance to APN than scheme 6, and is the preferred calibration scheme.

### *D. The Effects of Clutter and Noise on Calibration Accuracy*

The analysis in previous sections has implicitly assumed that the calibrators can be constructed and located in such a way that noise and clutter can be neglected. However, the 6 MHz bandwidth allowable under ITU regulations for a spaceborne P-Band SAR corresponds to a slant range spatial resolution of 25 m, or 50 m ground range resolution at an incidence angle of $30^o$. Hence, to keep the clutter to an acceptable level, the areas of low backscatter surrounding the calibrators need be quite large. To assess how critical this requirement is, or equivalently how large the Signal to Noise Ratio (SNR) needs to be, the performance of the calibration was evaluated for different levels of SNR.

Under the assumption of no APN error, Fig.14 shows the standard deviation (SD) of the FR estimation error and the amplitude and phase estimation errors of the radar system errors for scheme 5 (the preferred scheme) as a function of SNR (assuming the clutter and noise are white Gaussian), calculated from 100,000 Monte Carlo simulations for each value of SNR ranging from 20 dB to 60 dB in steps of 1 dB. As long as the SNR exceeds 40 dB, noise has little impact on the estimation of FR, channel imbalance $f$ and cross-talk $\delta_c$, but it has marked effects on the cross-talk terms $\delta_1$ and $\delta_2$, especially $\delta_1$. For example, an SNR of 40 dB leads to an FR error whose SD is 0.52°, errors in the amplitude of $f$ and $\delta_c$ with SD about 0.15 dB, and errors in the phase of $f$ and $\delta_c$ with SD about 1°, while for $\delta_1$ and $\delta_2$ the SDs of the errors are respectively 1.83 dB and 0.53 dB for amplitude, and 12.15° and 3.51° for phase. An SNR of at least 50 dB seems necessary to reduce the phase error in $\delta_1$ to tolerable levels, which gives some guide to the required size of the passive calibrators, the performance of the active calibrators and the dimensions of the low backscatter background on which they must be positioned.

## V. CONCLUSIONS

Spaceborne SAR systems are much more stable in time and space than airborne systems, and have

less need of frequent calibration. Therefore, precise measurements of system errors at a small number of selected sites by a scheme that removes FR effects is likely to be sufficient for a spaceborne CTLR mode CP SAR system.

This paper has proposed a number of possible calibration schemes to provide these measurements, all of which involve a mixture of passive and active calibration devices, although the passive devices could be replaced with active devices with the same polarimetric signatures. It establishes that calibration strategies involving four devices yield more accurate estimates of the radar system parameters than those using just three devices, though incur greater cost and complexity in deployment. It has also established that gridded trihedrals give significant advantages over the dihedral and trihedral, because of their much lower APN and insensitivity to pointing accuracy. On the negative side, gridded trihedrals require accurate construction of the grid, and the microwave absorber layer is likely to be affected by rain [22]; these problems can be avoided if equivalent active devices are employed. A preferred calibration scheme emerges clearly from the analysis and simulations, involving four polarimetric selective calibrators, namely, two gridded trihedrals (or active calibrators) that select for the HH and VV channels and two active calibrators that select for the HV and VH channels. The optimal calibration algorithm provides accurate estimates of all the radar system parameters, whatever the Faraday rotation conditions. It also provides accurate estimates of Faraday rotation itself.

As regards deployment, the compact polarimetric configuration is aimed at realizing wide swaths, over which the system performance may change. Hence several sets of mixed calibrators would need to be positioned across the swath, though not all sets would need to be contained in the same image.

## REFERENCES

[1] H. Balzter, M. Davidson, T. Le Toan, P. Paillou, K. Papathanassiou, S. Plummer, S. Quegan, F. Rocca, S. S. Saatchi, H. Shugart and L. Ulander, “BIOMASS Report for Assessment”, ESA SP 1313/2, European Space Agency 2008.

[2] W. B. Gail, “Effect of Faraday rotation on polarimetric SAR,” *IEEE Trans. Aerosp. Electron. Syst.*, vol. 34, no. 1, pp. 301–308, Jan. 1998.

[3] Z.-W. Xu, J. Wu, and Z.-S. Wu, “A survey of ionospheric effects on space-based radar,” *Waves in Random Media*, vol. 14, no. 12, pp. 189-272, Apr. 2004.

[4] F. J. Meyer and J. B. Nicoll, “Prediction, detection, and correction of Faraday rotation in full-polarimetric L-band SAR data,” *IEEE Trans. Geosci. Remote Sens.*, vol. 46, no. 10, pp. 3076-3086, Oct. 2008.

[5] J.-C. Souyris, P. Imbo, R. Fjørtoft, S. Mingot, and J.-S. Lee, “Compact polarimetry based on symmetry properties of geophysical media: The π/4 mode,” *IEEE Trans. Geosci. Remote Sens.*, vol. 43, no. 3, pp. 634–646, Mar. 2005.

[6] J. C. Souyris, N. Stacy, T. Ainsworth, J. S. Lee, and P. Dubois-Fernandez, “SAR compact polarimetry for Earth observation and planetology: Concepts and challenges, A study case at P band” *Proc. POLINSAR*, Frascati, Italy, 2007.

[7] R. K. Raney, “Dual-polarized SAR and stokes parameters,” *IEEE Geosci. Remote Sens. Lett.*, vol. 3, no. 3, pp. 317–319, Jul. 2006.

[8] R. K. Raney, “Hybrid-polarity SAR architecture,” *IEEE Trans. Geosci. Remote Sens.*, vol. 45, no. 11, pp. 3397-3404, Nov. 2007.

[9] N. Stacy and M. Preiss, “Compact polarimetric analysis of X-band SAR data,” *Proc. EUSAR* 2006, Dresden, 16-18 May, 2006 (on CDROM).

[10] P. Dubois-Fernandez, S. Anglliaume, J. C. Souyris, F. Garestier, and I. Champion, “The specificity of P-band PolINSAR data over vegetation,” *Proc. POLINSAR 2007*, Frascati, Italy, Jan. 2007.

[11] P. Dubois-Fernandez, J.C. Souyris, S. Angelliaume, and F. Garestier, “The compact polarimetry alternative for spaceborne SAR at low frequency,” *IEEE Trans. Geosci. Remote Sens.*, vol. 46, no. 10, pp. 3208–3222, Oct. 2008.

[12] M. E. Nord, T. L. Ainsworth, J.-S. Lee, and N. J. S. Stacy, “Comparison of compact polarimetric Synthetic Aperture Radar Modes,” *IEEE Trans. Geosci. Remote Sens.*, vol. 47, no. 1, pp. 174–188, Jan. 2009.

[13] M. Truong-Loï, A. Freeman, P. Dubois-Fernandez, and E. Pottier, “Estimation of soil moisture and Faraday rotation from bare surfaces using compact polarimetry”, *IEEE Trans. Geosci. Remote Sens.*, vol. 47, no. 11, pp. 3608–3615, Nov. 2009.

[14] A. Freeman, P. Dubois-Fernandez and My-Linh Truong-Loï, “Compact polarimetry at longer wavelengths – calibration,” *Proc. EUSAR 2008*, Graf-Zeppelin-Haus, 2-5 June, 2008. (on CDROM).

[15] P. A. Wright, S. Quegan, N. S. Wheadon, and C. D. Hall, “Faraday rotation effects on L-band spaceborne data,” *IEEE Trans. Geosci. Remote Sens.*, vol. 41, no. 12, pp. 2735-2744, Dec. 2003.

[16] A. Freeman, Y. Shen, C.L. Werner, “Polarimetric SAR calibration experiment using active rad*ar calibrators,” IEEE Trans. Geosci. Remote Sens.*, vol. 28, no. 7, pp.224-240, Mar. 1990.

[17] M. Fujita, “Development of a Retrodirective PARC for ALOS/PALSAR calibration,” *IEEE Trans. Geosci. Remote Sens.*, vol. 41, no. 10, pp. 2177-2186, Oct. 2003.

[18] M. Fujita, “Polarimetric calibration of space SAR data subject to Faraday rotation – a three target approach,” *Proc. IEEE IGARSS 2005*, vol.8, pp. 5497-5500, 25-29 July 2005.

[19] M. Fujita, T. Masuda,Y. Fujino, and M. Satake, “Polarimetric calibration of the SIR-C C-band channel using active radar calibrators and polarization selective dihedrals,” *IEEE Trans. Geosci. Remote Sensing*, vol. 36, pp. 1872–1878, Nov. 1998.

[20] S. H. Yueh, J. A. Kong, R. M. Barnes, and R. T. Shin, "Calibration of polarimetric radars using in-scene reflectors," *Progress In Electromagnetics Research, PIERS 03*, pp. 451-510, 1990.

[21] D. R. Sheen, E. L. Johansen, L. P. Elenbogen, and E. S. Kasischke, "The gridded trihedral: a new polarimetric SAR calibration reflector," *IEEE Trans. Geosci. Remote Sens.*, vol. 30, no. 6, pp. 1149-1153, Nov. 1992.

[22] M. Lavalle, B. Rosich, T. Ainsworth, E. Pottier, and D. Solimini, "Calibration of dual-pol SAR data: a possible approach for Sentinel-1," *Proc. POLINSAR 2009*, Frascati, Italy, Jan. 2009.

[23] M. Sekido, T. Kondo, E. Kawai, and M. Imae, "Evaluation of GPS-based ionospheric TEC map by comparing with VLBI data," *Radio Sci.*, vol. 38, no. 4, pp. 8-1–8-22, Jul. 2003.

[24] L. Mandrake, B. Wilson, C. Wang, G. Hajj, A. Mannucci, and X. Pi, "A performance evaluation of the operational Jet Propulsion Laboratory/University of Southern California Global Assimilation Ionospheric Model (JPL/USC GAIM)," *J. Geophys. Res.*, 110, A12306, doi:10.1029/2005JA011170. Dec. 2005.

[25] J. Chen and S. Quegan, "Improved estimators of Faraday rotation in spaceborne polarimetric SAR data," *IEEE Geosci. Remote Sens. Lett*, vol. 7, no. 4, pp. 846-850, Oct. 2010.

**ACKNOWLEDGEMENTS:**

This work described in the paper was supported in part by the National Science Foundation of China (NSFC) under Grant 60602045, and in part by the Fundamental Research Funds for the Central Universities, China under Grant YWF-10-01-A24. The authors would like to appreciate the anonymous reviewers for their perceptive comments and suggestions, which significantly helped us to improve the paper.

**Jie Chen (M'06)** received the B.S. and Ph.D. degrees in information and communication engineering from Beihang University (Beijing University of Aeronautics and Astronautics, BUAA), Beijing, China,

in 1996 and 2002, respectively. His Ph.D. study was concerned with spaceborne synthetic aperture radar (SAR) system modeling and signal processing.

He is an associate professor with the School of Electronics and Information Engineering, Beihang University (BUAA) from 2004. He has published over 40 journal and conference papers. He was awarded New Century Excellent Talents in University, (NCET), by Ministry of Education, China, in 2006, and Excellent Young Teachers in University, by Fok Ying Tong Education Foundation and Ministry of Education, China, in 2008, respectively.

His current research interests include remote sensing information acquisition and signal processing; topside ionosphere exploration based on spaceborne HF-SAR; high-resolution spaceborne SAR image formation; modeling and simulation for spaceborne SAR systems.

He is a Visiting Researcher at the School of Mathematics and Statistics, University of Sheffield, Sheffield, UK, from February 2009 to January 2010, working with Prof. Shaun Quegan on ionospheric effects on low frequency space radars that measure forest biomass and ionospheric electron densities.

**Shaun Quegan** (M'90) received the B.A. and M.Sc. degrees in mathematics from the University of Warwick, Warwick, U.K., in 1970 and 1972, respectively, and the Ph.D. degree from the University of Sheffield, Sheffield, U.K., in 1982. His Ph.D. study was concerned with ionospheric modeling.

Between 1982 and 1986, he was a Research Scientist at the Marconi Research Centre, and led the Remote Sensing Applications Group from 1984 to 1986. He established the SAR Research Group at the University of Sheffield in 1986, whose success led to his Professorship awarded in 1993. In the same year he helped to inaugurate the Sheffield Centre for Earth Observation Science, of which he remains the Director. In 2001, he became the Director of the U.K. National Environmental Research Council Centre for Terrestrial Carbon Dynamics (CTCD), which is concerned with assimilating Earth

observation (EO) and other data into process models of the land component of the carbon cycle. He was a member of the ESA Earth Science Advisory Committee and is Chairman of the BIOMASS Mission Assessment Group. His broad interests in the physics, systems and data analysis aspects of radar remote sensing are now subsumed in the more general aim of exploiting EO technology to meet the needs of carbon cycle science.

TABLE I

STATISTICAL ANALYSIS OF AMPLITUDE AND PHASE ERRORS CORRESPONDING TO THE OPTIMAL CHANNEL IMBALANCE AND CROSS-TALK ESTIMATES IN FIGS.2-9

| | Amplitude Error (dB) | | Phase Error (deg) | |
|---|---|---|---|---|
| | Mean | RMS | Mean | RMS |
| $\hat{f}$ | -0.0561 | 0.00434 | 0 | 0.102 |
| $\hat{\delta}_1$ | -2.523 | 1.5938 | 1.001 | 1.259 |
| $\hat{\delta}_2$ | 0 | 0 | 0 | 0 |
| $\hat{\delta}_c$ | 0.0432 | 0 | 1.179 | 0 |

TABLE II

STATISTICAL ANALYSIS OF ESTIMATED FR ERRORS CORRESPONDING TO FIG.10 WITH DIFFERENT PHASE IMBALANCE VALUES

| | arg{$f$}=0 | | arg{$f$}=π/3 | |
|---|---|---|---|---|
| | Mean | RMS | Mean | RMS |
| $\hat{\Omega}_1^{\text{(Original)}}$ | -1.907 | 0 | -1.179 | 0 |
| $\hat{\Omega}_2^{\text{(Original)}}$ | -0.422 | 3.462 | 0.578 | 3.088 |
| $\hat{\Omega}_2^{\text{(Modified)}}$ | 2.855 | 0.177 | 2.856 | 0.409 |
| $\hat{\Omega}^{\text{(Optimal)}}$ | 0.472 | 0.542 | 0.892 | 0.445 |

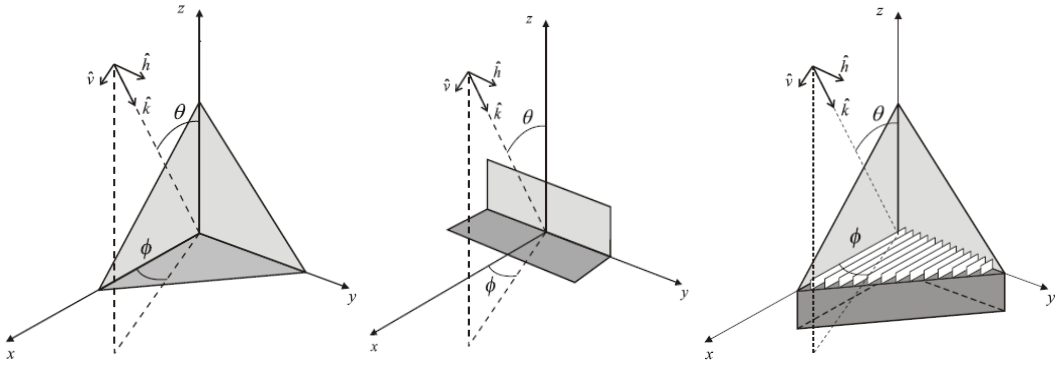


(a) Trihedral (b) Dihedral (c) Gridded trihedral

Fig. 1 The passive calibrators.

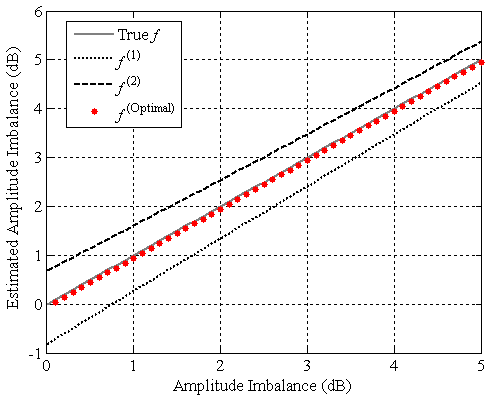


Fig. 2 Simulation of channel amplitude imbalance estimation (arg{$f$} = π/3, $|\delta_1| = |\delta_2| = 0.1$, $|\delta_c| = 0.32$, arg{$\delta_1$}= arg{$\delta_2$}= arg{$\delta_c$}=0, Ω = π/4).

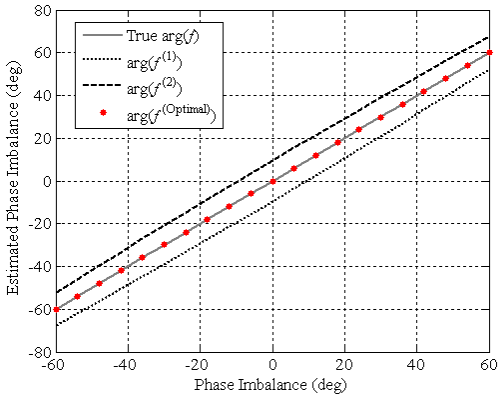


Fig. 3 Simulation of channel phase imbalance estimation ($|f| = 1.5$, $|\delta_1| = |\delta_2| = 0.1$, $|\delta_c| = 0.32$, arg{$\delta_1$}= arg{$\delta_2$}= arg{$\delta_c$}=0, Ω = π/4).

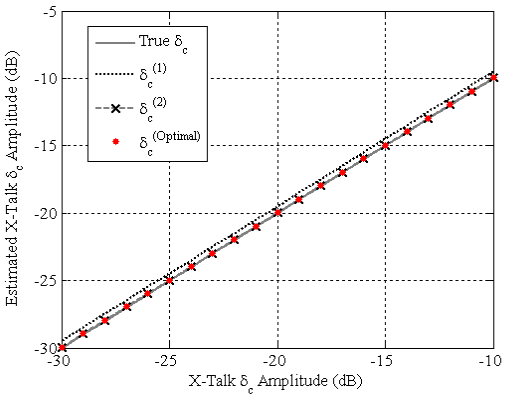


Fig. 4 Simulation of estimating cross-talk $\delta_c$ amplitude ($|f| = 1.5$, arg{$f$} = π/3, $|\delta_1| = |\delta_2| = 0.1$, arg{$\delta_1$}= arg{$\delta_2$}= arg{$\delta_c$}=0, Ω = π/4)

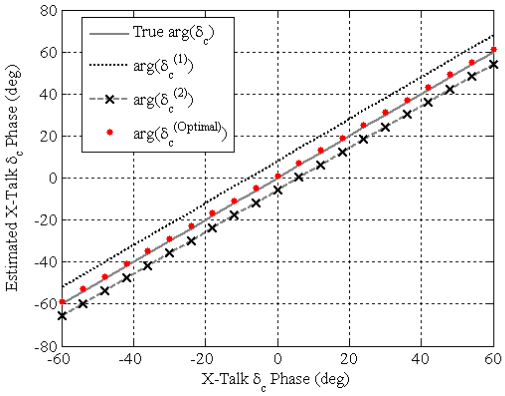


Fig. 5 Simulation of estimating cross-talk $\delta_c$ phase ($|f| = 1.5$, arg{$f$} = π/3, $|\delta_1| = |\delta_2| = 0.1$, $|\delta_c| = 0.32$, arg{$\delta_1$}= arg{$\delta_2$}= 0, Ω = π/4)

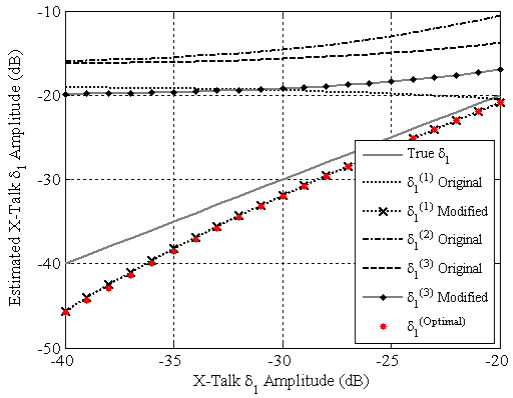


Fig. 6 Simulation of estimating cross-talk $\delta_1$ amplitude ($|f| = 1.5$, $\arg\{f\} = \pi/3$, $|\delta_2| = 0.1$, $|\delta_c| = 0.32$, $\arg\{\delta_1\} = \arg\{\delta_2\} = \arg\{\delta_c\} = 0$, $\Omega = \pi/4$).

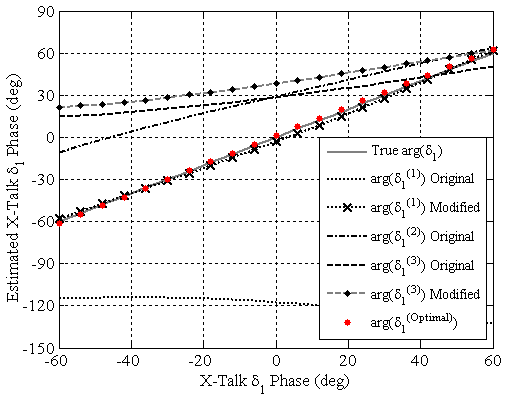


Fig.7 Simulation of estimating cross-talk $\delta_1$ phase ($|f| = 1.5$, $\arg\{f\} = \pi/3$, $|\delta_1| = |\delta_2| = 0.1$, $|\delta_c| = 0.32$, $\arg\{\delta_2\} = \arg\{\delta_c\} = 0$, $\Omega = \pi/4$).

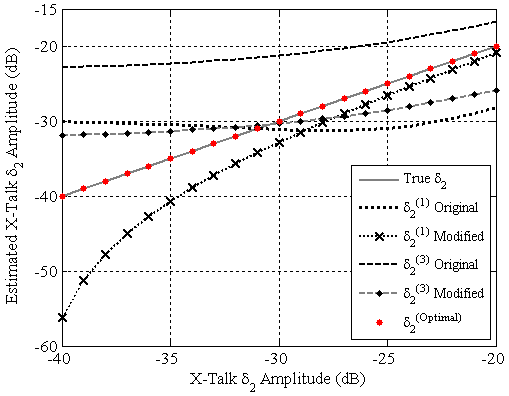


Fig. 8 Simulation of estimating cross-talk $\delta_2$ amplitude ($|f| = 1.5$, $\arg\{f\} = \pi/3$, $|\delta_1| = 0.1$, $|\delta_c| = 0.32$, $\arg\{\delta_1\} = \arg\{\delta_2\} = \arg\{\delta_c\} = 0$, $\Omega = \pi/4$).

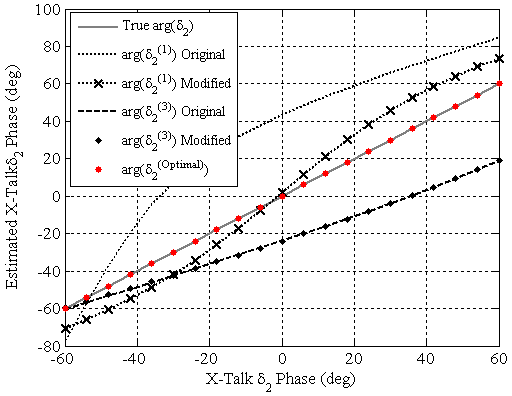


Fig. 9 Simulation of estimating cross-talk $\delta_2$ phase ($|f| = 1.5$, $\arg\{f\} = \pi/3$, $|\delta_1| = |\delta_2| = 0.1$, $|\delta_c| = 0.32$, $\arg\{\delta_1\} = \arg\{\delta_c\} = 0$, $\Omega = \pi/4$).

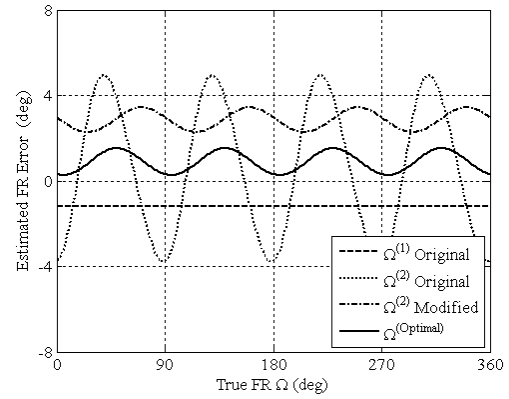


(a)

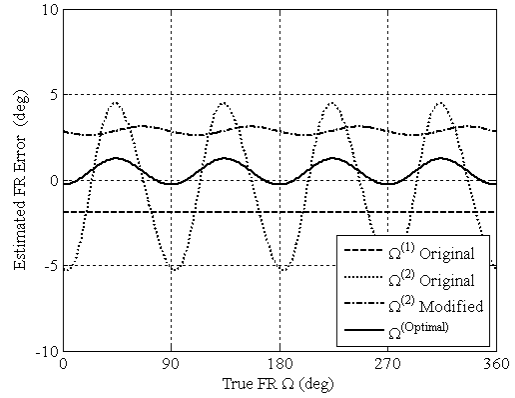


(b)

Fig. 10 Simulation of the estimated FR error as a function of true FR angle, with $|f| = 1.5$, $|\delta_1| = |\delta_2| = 0.1$, $|\delta_c| = 0.32$, $\arg\{\delta_1\} = \arg\{\delta_2\} = \arg\{\delta_c\} = 0$, but different phase imbalance values: (a) $\arg\{f\} = \pi/3$, (b) $\arg\{f\} = 0$.

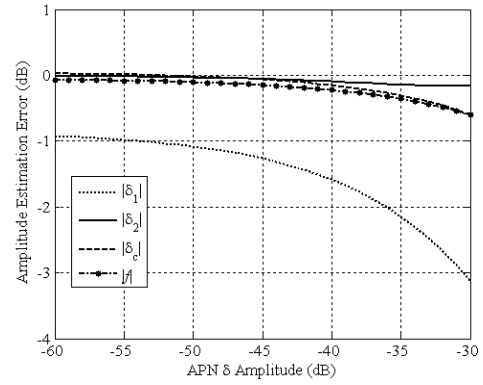


(a)

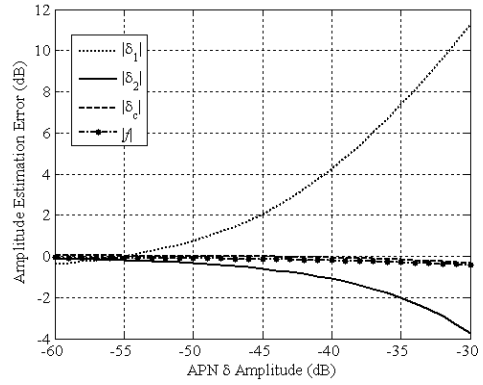


(b)

Fig. 11 Comparison of estimated channel imbalance and cross-talk amplitude errors derived by (a) Scheme 5 and (b) Scheme 6 as a function of APN amplitude, $|\delta|$, with $|f| = 1.5$, $\arg\{f\} = \pi/3$, $|\delta_1| = |\delta_2| = 0.1$, $|\delta_c| = 0.32$, $\arg\{\delta_1\} = \arg\{\delta_2\} = \arg\{\delta_c\} = 0$, $\Omega = \pi/4$, $\arg\{\delta\} = 0$, $\delta_{Di} = \sqrt{10}\,\delta$.

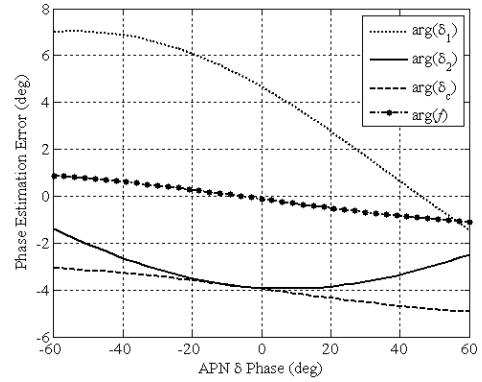


(a)

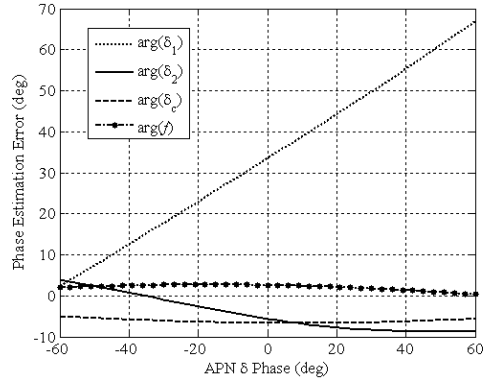


(b)

Fig. 12 Comparison of estimated channel imbalance and cross-talk phase errors derived from (a) Scheme 5 and (b) Scheme 6 as a function of APN phase, $\arg\{\delta\}$, with $|f| = 1.5$, $\arg\{f\} = \pi/3$, $|\delta_1| = |\delta_2| = 0.1$, $|\delta_c| = 0.32$, $\arg\{\delta_1\} = \arg\{\delta_2\} = \arg\{\delta_c\} = 0$, $\Omega = \pi/4$, $|\delta| = -40$ dB, $\delta_{Di} = \sqrt{10}\,\delta$.

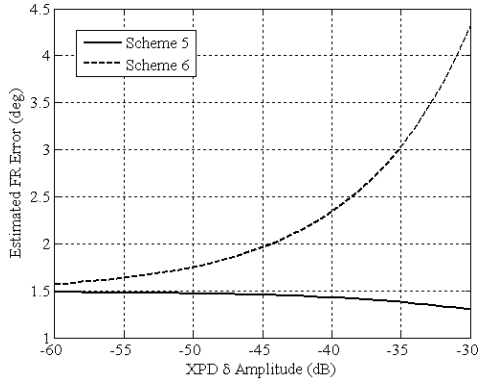


(a)

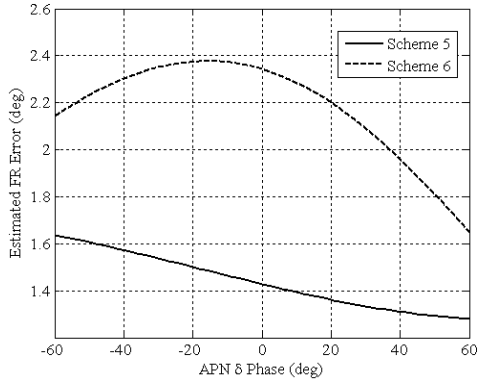


(b)

Fig. 13 Comparison of the estimated FR errors from Schemes 5 and 6 as a function of (a) amplitude ($\arg\{\delta\} = 0$) and (b) APN phase ($|\delta| = -40$dB), with $|f| = 1.5$, $\arg\{f\} = \pi/3$, $|\delta_1| = |\delta_2| = 0.1$, $|\delta_c| = 0.32$, $\arg\{\delta_1\} = \arg\{\delta_2\} = \arg\{\delta_c\} = 0$, $\Omega = \pi/4$, $\delta_{Di} = \sqrt{10}\,\delta$.

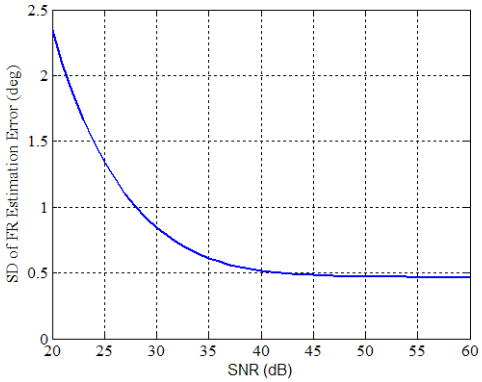


(a)

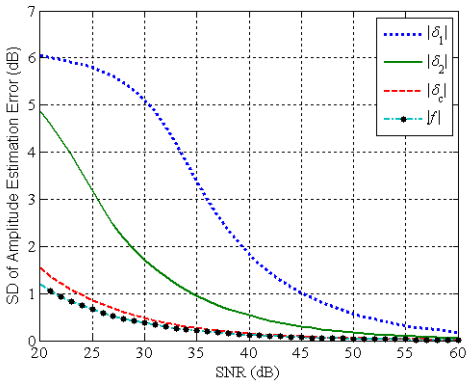


(b)

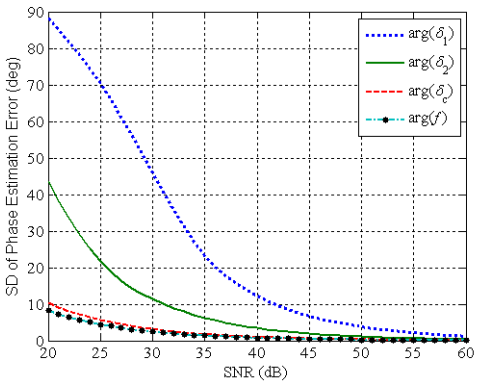


(c)

Fig. 14 SD of FR estimation error, amplitude an phase estimation errors of channel imbalance and cross-talks for Scheme 5 as a function of SNR, under the conditions of no APN error (i.e. $\delta = 0$), and $|f| = 1.5$, $\arg\{f\} = \pi/3$, $|\delta_1| = |\delta_2| = 0.1$, $|\delta_c| = 0.32$, $\arg\{\delta_1\} = \arg\{\delta_2\} = \arg\{\delta_c\} = 0$, $\Omega = \pi/4$.

(a) FR estimation error; (b) amplitude errors of channel imbalance and cross-talks; (c) phase errors of channel imbalance and cross-talks.